Nanoparticle-Induced Charge Redistribution of the Air−Water Interface

Amaia Beloqui Redondo,[†] Inga Jordan,[‡] Ibrahim Ziazadeh,[§] Armin Kleibert,[∥] Javier B. Giorgi,[⊥] Hans Jakob Wörner,[‡] Sylvio May,[#] Zareen Abbas,[§] and Matthew A. Brown*,[†,∇]

[†]Institute for Chemical and Bioengineering, ETH Zürich, CH-8093 Zurich, Switzerland

[‡]Laboratory of Physical Chemistry, ETH Zürich, CH-8093 Zurich, Switzerland

[§]Department of Chemistry and Molecular Biology, University of Gothenburg, SE-41296 Gothenburg, Sweden

[∥]Paul Scherrer Institute, CH-5232 Villigen PSI, Switzerland

[⊥]Center for Catalysis Research and Innovation, Department of Chemistry, University of Ottawa, Ottawa, Ontario K1N 6N5, Canada

[#]Department of Physics, North Dakota State University, Fargo, North Dakota 58108-6050, United States

[∇]Laboratory for Surface Science and Technology, Department of Materials, ETH Zürich, CH-8093 Zurich, Switzerland

S *Supporting Information*

ABSTRACT: The air−water interface is believed to carry a negative electrostatic potential that is nontrivial to invert through pH, electrolyte, or electrolyte strength. Here, through a combined experimental and theoretical study, we show that the close approach of a negatively charged nanoparticle induces a charge redistribution of the air−water interface. Using different electrolytes to control the interfacial potential of the nanoparticles, X-ray photoelectron spectroscopy (XPS) results establish that nanoparticles with a more negative zeta potential adsorb closer to the air−water interface than do the same particles with a less negative zeta potential. The short-ranged attractive force between two (nominally) negative surfaces is caused by charge redistribution under the strong electric field of the nanoparticle that locally inverts the charge density of the air−water interface from negative to positive. The nature of the nanoparticle's counterions modulates the attractive interaction, which thus could be used to control reactivity, stability, and nanoparticle self-assembly at air−water interfaces.
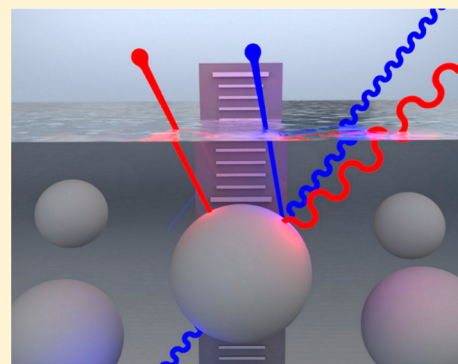
INTRODUCTION

The attachment of nanoparticles (NPs) at liquid interfaces is well established for stabilizing and increasing the lifetimes of emulsions, foams, and microbubbles[1−3] and has recently emerged as a promising strategy in nanotechnology[4,5] for the controlled assembly of hierarchical two- and three-dimensional nanocrystal superlattices that possess unique chemical and physical properties. Control over the interface affinity of NPs in solutions can be realized to a large extent by tuning their size and the chemical characteristics of their ligands,[6] and is traditionally characterized by surface tension measurements that rely on the Gibbs adsorption equation.[7] However, despite the relative simplicity of a surface tension measurement and its widespread use, the interpretation of the result is not straightforward,[8] and the lack of chemical and depth resolution preclude, except in the most trivial of cases, a complete microscopic description of NP attachment at and near liquid interfaces.[9,10] As a result, the underlying molecular mechanisms that regulate NP spatial distributions at liquid interfaces remain largely speculative.[9−11]

For systems in which the NPs are charged, the electrostatic state of the liquid interface is expected to play a significant role in regulating spatial distributions, but its effect is far from understood. The air−water interface (AWI), which commonly serves as a model for aqueous−hydrophobic interfaces, is believed to carry a negative electrostatic potential with respect to bulk water that results from the dipole (and higher-order) potential due to ordered water at the AWI and (or) from preferential adsorption of anions (e.g., OH⁻ from the auto dissociation of water) in concentrations that exceed that in the bulk.[12] Uncertainty, however, exists in the sign of the potential at the AWI, let alone its exact magnitude,[12] which makes quantitatively predicting its role in regulating NP spatial distributions difficult. Here we use in situ X-ray photoelectron spectroscopy (XPS) to elucidate the consequences of the interplay between NP and AWI surface potentials for regulating NP spatial distributions. We quantitatively measure the spatial distributions of oxide NPs near the AWI in different alkali chloride electrolytes (Figure 1a) and show that the more negative the charge of the NP the closer it approaches the AWI.
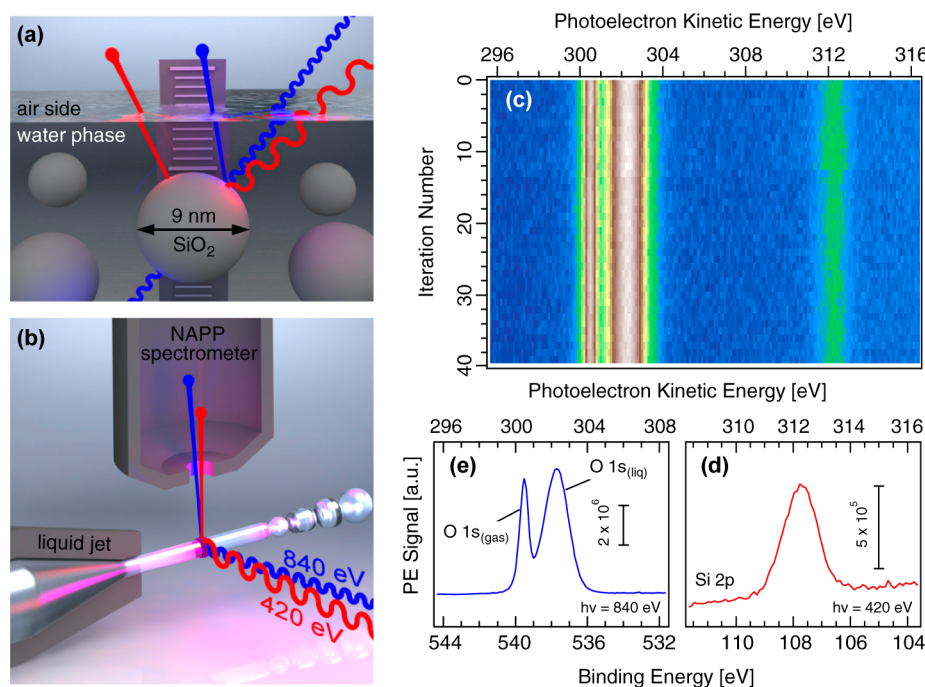
Figure 1. (a) Spatial distributions of nanoparticles at the air−water interface as a function of electrolyte are determined using X-ray photoelectron spectroscopy. (b) Colloidal suspensions are injected into the vacuum measurement chamber using a fused quartz nozzle of 32 μm diameter. The photon energy of the synchrotron beam is set at 420 eV to ionize the Si 2p orbital. Second-order radiation, 840 eV, is used to simultaneously measure O 1s photoemission. Measuring the Si 2p and O 1s orbitals within 10 eV photoelectron kinetic energy (pKE) ensures a constant probe depth of the experiment. (c) Raw data collected for 5 wt % SiO$_2$ in 50 mM NaCl electrolyte. The PE map is integrated for each pKE to yield the spectra of panels d and e. (d) Integrated Si 2p region showing a single component. The binding energy scale is calculated using incident photon energy of 420 eV. (e) Integrated O 1s region shows two components that are assigned as O 1s(gas) and O 1s(liq).[15] The binding energy scale is calculated using incident photon energy of 840 eV. The gas-phase component arises because of a mismatch in the cross section of the photon beam (ca. 60 μm fwhm) and the liquide microjet diameter (32 μm).[16]

This electrostatic attraction to the AWI of higher charged negative NPs is attributed to a NP-induced charge redistribution of the AWI that inverts its negative charge density to positive. Our work suggests that in the presence of a negatively charged NP with high surface charge density the AWI will carry a positive surface charge at short separations; therefore, an *attractive* electrostatic interaction will emerge. Although the present work applies to colloidal silica (SiO$_2$), the similarities between charge-stabilized NPs and proteins, the latter of which also contain a high density of charged groups (often at the active site),[13] means our insights are expected to extend well beyond that of soft-matter colloidal nanoscience and have direct consequences on the properties of protein films at liquid−hydrophobic interfaces[14] and should create new opportunities in self-assembly for applications in chemistry, nanotechnology, and nanomedicine.

■ METHODS

All experiments were carried out using Ludox SM-30 colloidal silica (Sigma-Aldrich). Aqueous suspensions of the desired wt % silica in 50 mM LiCl, NaCl, KCl, and CsCl (Sigma-Aldrich, ACS Reagent grade, used as-received) were prepared using Milli-Q water. Small-angle X-ray scattering (SAXS), X-ray diffraction (XRD), X-ray photoelectron spectroscopy (XPS), and surface tension experiments used 5.0 wt % suspensions (dried in the case of XRD); transmission electron microscopy (TEM) used 0.3 wt % (again dried); and the electrophoretic mobility experiments (zeta potential) were done using 2.0 wt % suspensions. Complete details of the TEM, SAXS, XRD, surface

tension, XPS, and electrophoretic mobility measurements are included in the Supporting Information.

Debye−Hückel Theory. When the surface of a negatively charged NP with surface charge density σ_{NP} approaches the AWI, its diffuse layer of counterions interacts electrostatically with the planar AWI. Because the Debye screening length is small, $l_D = 13$ Å at 50 mM monovalent electrolyte compared to the 9 nm particles, the electrostatic NP−AWI interaction can be approximated as being that between two planar parallel surfaces, both of area A separated by a distance D from one another. It is most instructive to consider this interaction within the Debye−Hückel model, in which the electrostatic potential, $\Phi(x)$, satisfies the linearized Poisson−Boltzmann equation, $l_D^2\Phi'' = \Phi$. A prime denotes the derivative with respect to the spatial coordinate x. Because the AWI is widely regarded to carry a fixed negative potential of about $\Phi_{AWI} = -50$ mV, the linearized Poisson−Boltzmann equation, with the AWI located at $x = 0$ and the NP at $x = D$, has to fulfill the boundary conditions $\Phi(x = 0) = \Phi_{AWI}$ and $\Phi'(x = D) = \Phi_{NP}/l_D$, where $\Phi_{NP} = l_D\sigma_{NP}/(\varepsilon_0\varepsilon_W)$ is the surface potential of the NP in bulk water and ε_0 and ε_W denote the permittivity in vacuum and the dielectric constant in water, respectively. From the solution

$$\Phi(x) = \left[\Phi_{AWI}\cosh\left(\frac{D-x}{l_D}\right) + \Phi_{NP}\sinh\left(\frac{x}{l_D}\right)\right]/\cosh(D/l_D) \tag{1}$$

we can calculate the electrostatic free energy from products of the potential and its derivative at each surface according to[17]
$F_{el}/A = (\varepsilon_0\,\varepsilon_W[\Phi(0)\,\Phi'(0) + \Phi(D)\,\Phi'(D)])/2$.

Table 1. Summary of the XPS Si 2p/O 1s(liq) Ratios, Surface Pressures, Zeta Potentials, and in Situ SAXS and TEM Results for Colloidal Silica (SiO$_2$) in 0.05 M Aqueous Suspensions of LiCl, NaCl, KCl, and CsCl

electrolyte (50 mM)	Si 2p/O 1s(liq) ratio[a,b] (arb. units)	pH (±0.1)	surface pressure[a,b] (mN/m)	zeta potential[a,c] (mV)	SAXS[b] (nm)	TEM[d] (nm)
LiCl	1.0 (0.03)	10.0	0.10 (0.03)	−53.8 (3.3)	8.7 (2.1)	9.2 (1.5)
NaCl	0.85 (0.04)	10.0	0.13 (0.05)	−48.5 (4.2)	9.2 (1.9)	9.0 (1.6)
KCl	0.83 (0.03)	10.0	0.14 (0.05)	−44.5 (4.5)	9.1 (1.8)	9.0 (1.4)
CsCl	0.61 (0.04)	9.9	0.11 (0.06)	−40.0 (4.1)	9.4 (1.8)	9.2 (1.4)

[a]Error represents the standard deviation of repeat measurements. [b]5.0 wt % suspensions measured in solution. [c]2.0 wt % suspensions measured in solution. [d]0.3 wt % suspensions measured in vacuum after drying a drop of the suspension on a TEM grid.
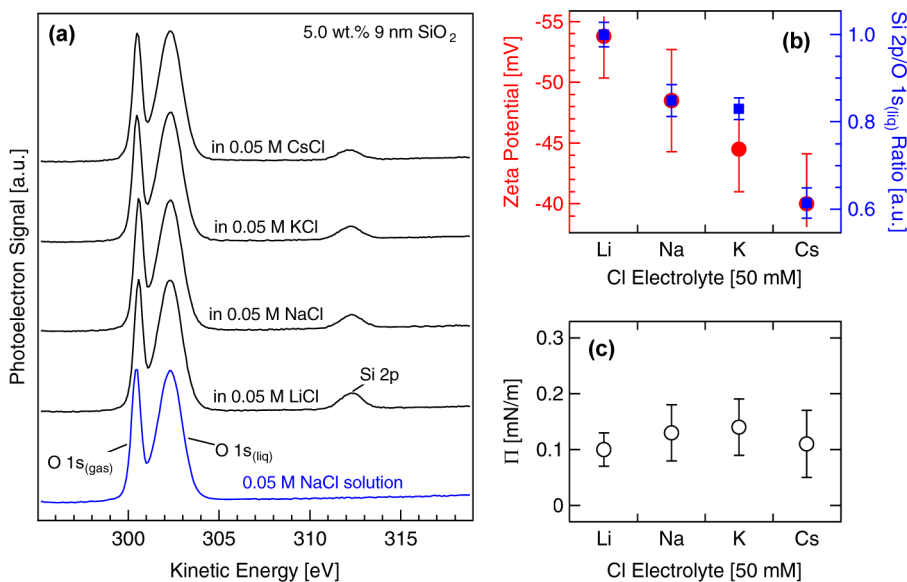

Figure 2. (a) O 1s and Si 2p XP spectral regions for 0.05 M NaCl (no NPs) and suspensions of SiO$_2$ in 50 mM LiCl, NaCl, KCl, and CsCl electrolytes. (b) Integrated Si 2p/O 1s(liq) PE ratios (blue squares) and zeta potentials (red circles). (c) Surface pressure of 5.0 wt % colloidal silica in 50 mM electrolyte suspensions. Error bars represent the standard deviation of repeat measurements.

Using eq 1 then yields

$$\frac{F_{el}}{A} = \left(\frac{\varepsilon_0 \varepsilon_W}{l_D}\right)\left[\frac{\Phi_{NP}\Phi_{AWI}}{\cosh\left(\frac{D}{l_D}\right)} + \left(\frac{1}{2}\right)(\Phi_{NP}^2 - \Phi_{AWI}^2)\tanh\left(\frac{D}{l_D}\right)\right] \tag{2}$$

as a function of the separation, D, between the two parallel surfaces. If Φ_{NP} and Φ_{AWI} carry the same sign and $|\Phi_{NP}| > |\Phi_{AWI}|$, there exists a distance $\bar{D} = l_D \log(\Phi_{NP}/\Phi_{AWI})$ that separates electrostatic attraction (for $D < \bar{D}$) from repulsion (for $D > \bar{D}$). The distance $\bar{D}$ is always smaller than the distance $\tilde{D} = l_D \operatorname{arcsinh}(\Phi_{NP}/\Phi_{AWI})$ at which the charge density at the AWI changes its sign. Hence, the attraction for $D < \bar{D}$ is a consequence of NP-induced charge reversal, from a negative charge density $\sigma_{AWI} = \varepsilon_0\varepsilon_W\Phi_{AWI}/l_D$ in the absence of the NPs to a positive charge density $\sigma_{AWI} = -\sigma_{NP} + \varepsilon_0\varepsilon_W\Phi_{AWI}D/l_D^2$ for NP−AWI separations of $D \ll l_D$. We point out that the energy barrier corresponding to the repulsive region $D > \bar{D}$ is $\Delta F_{el} = F_{el}(D = \bar{D}) - F_{el}(D \to \infty) = A((\varepsilon_0\varepsilon_W)/(l_D))\Phi_{AWI}^2$. For an effective area $A = (6\ nm)^2$ as well as $l_D = 13$ Å, $\Phi_{AWI} = -50$ mV, and $\varepsilon_W = 80$, this amounts to $\Delta F_{el} \approx 10k_BT$ (where k_B is the Boltzmann constant and T the absolute temperature) for a single NP at room temperature. For separations $D \ll l_D$, the free energy in eq 2 reduces to the simple expression

$$\frac{F_{el}}{A} = \left(\frac{\varepsilon_0 \varepsilon_W}{2l_D^2}\right)(\Phi_{NP}^2 - \Phi_{AWI}^2)D + \text{const} \tag{3}$$

The squared dependence of Φ_{AWI} in eq 3 renders the sign (negative or positive) of Φ_{AWI} arbitrary in the theoretical treatment, although as mentioned above experimental studies have shown that the AWI has negative potential.

To account for hydration forces an additional term that approximates the mutual perturbation of ordered water molecules close to the NP and AWI, $Be^{-D/\xi}$, where B is a positive constant and $\xi = 2.0$ Å is the characteristic decay length associated with the water ordering profile,[18] is added to the free energy. Minimizing the sum of the electrostatic free energy according to eq 3 and hydration free energy with respect to D yields the NP equilibrium distance according to eq 4 (below), where $z = \xi \log((\xi\varepsilon_0\varepsilon_W)/(2Bl_D^2))$ is a constant independent of Φ_{NP} and Φ_{AWI}. The magnitude of B is not known, and we therefore regard z as an unknown constant that provides a reference with respect to measuring D.

RESULTS

Colloidal Silica. Our experimental system consists of colloidal silica (SiO$_2$) in basic (pH 10) aqueous suspensions of 50 mM LiCl, NaCl, KCl, and CsCl. The particles are 9 nm in diameter as determined by ex situ (vacuum) transmission electron microscopy (TEM) (Figure S1a−f in Supporting Information and Table 1) and in situ small-angle X-ray

scattering (SAXS) (Figure S1g,h in Supporting Information and Table 1). X-ray diffraction measurements show a broad peak characteristic of amorphous silica[19] (Figure S1i in Supporting Information). These particles can be thought of as representing the broad class of hydroxyl (−OH) covered oxide surfaces found in geochemistry,[20] bio-nanotechnology,[21] nanomedicine,[22] and more general colloidal science.[23]

XPS from a Liquid Microjet. The NP suspensions are passed through a 32 μm liquid jet[24] (LJ) inside the ionization chamber of a near ambient pressure photoemission (NAPP) spectrometer[25] and spatially overlapped with synchrotron radiation (Figure 1b) from the Surface/Interface: Microscopy beamline[26] of the Swiss Light Source storage ring to collect photoelectron spectra (Figure 1c). The primary photon beam is set at 420 eV to collect Si 2p (binding energy (BE) = 108 eV[27]) photoelectron (PE) spectra at a photoelectron kinetic energy (pKE) of 312 eV (Figure 1d). The beamline optics provide simultaneous excitation with second-order radiation (840 eV) that allows for O 1s (BE = 538 eV[28]) spectra (Figure 1e) to be collected in the same pKE window as the Si 2p without having to move any optical element of the beamline. This novel approach for liquid-based XPS ensures uniform probe depth into solution for both orbitals. It also guarantees constant overlap of the incident X-rays and the LJ for both spectral regions and thereby greatly improves the reliability and reproducibility of the reported Si 2p/O 1s(liq) peak areas.

There are two peaks in the O 1s spectral region (Figure 1e). The one at lower pKE (higher BE) is assigned to gas-phase water from the background vapor in the ionization chamber, O 1s(gas), and the one at higher pKE (lower BE) from condensed water of the liquid microjet, O 1s(liq).[15] Spectral overlap with water prevents the oxygen component of the NPs from being detected.[29] A single component is present in the Si 2p region and assigned to SiO_2 NPs in suspension as evidenced by its absence in the spectrum of (reference water) 0.05 M NaCl (Figure 2a, bottom trace).

Nanoparticle Spatial Distributions at the AWI. The O 1s and Si 2p PE spectra from 5.0 wt % 9 nm SiO_2 in aqueous suspensions of 50 mM LiCl, NaCl, KCl, and CsCl are recorded in the pKE range of 300−315 eV (Figure 2a). The constant O 1s(gas) to O 1s(liq) ratio for all spectra demonstrates consistent overlap of the LJ with the X-rays during the course of the experiments. The ratio of the integrated PE peak areas, Si 2p/O 1s(liq), is determined following a standard background subtraction (blue squares of Figure 2b and Table 1). The ratio decreases as the molecular weight of the alkali chloride electrolyte is increased. This integrated ratio is directly related to the relative concentration of SiO_2 NPs within the fixed probe volume of the XPS experiment as the electrolyte is varied. That is, the local concentration of SiO_2 NPs near the AWI is a strong function of background electrolyte and follows according to LiCl > NaCl ≥ KCl > CsCl.

The relative immersion depths or different spatial distributions of the NPs at the AWI can be calculated from the XPS Si 2p/O 1s(liq) ratios for the different electrolytes. The geometry of the model (inset of Figure S2 in Supporting Information; see Supporting Information for complete details) is based on a well-established calculation that assumes an exponential decrease in XP signal intensity with increased NP distance below the AWI (Figure S2).[9,27] We use an electron inelastic mean free path (eIMFP) of 1.3 nm for both SiO_2[30] and H_2O.[31] A NP in LiCl electrolyte is assumed to have an arbitrary depth of zero (Figure 3) because its highest Si 2p/O 1s(liq) ratio
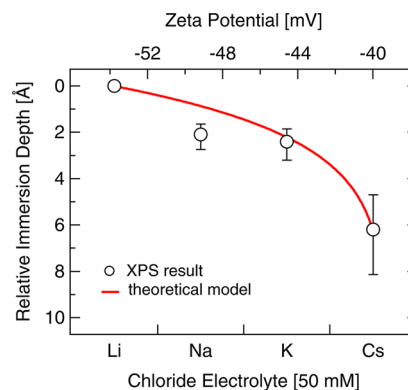

Figure 3. Calculated relative immersion depths in different electrolytes based on the experimental PE intensity ratios shown in Figure 2b plotted together with a theoretical prediction that employs the linear Debye−Hückel model. Current values for the eIMFP at ca. 300 eV KE in aqueous solution range from 1.0 to 1.7 nm, and the error bars span these values.

implies closest approach to the AWI. The immersion depths of the NPs in the other three electrolytes are calculated relative to this (Figure 3, open circles). We have accounted for the range of eIMFPs (1.0−1.7 nm) currently reported in the literature for liquid water at 300 eV KE[32,33] (error bars in Figure 3). On the basis of the decrease in the Si 2p/O 1s(liq) intensity ratio, a 9 nm particle in 50 mM NaCl electrolyte is calculated to have a relative immersion depth of 2.1 Å, 2.4 Å in 50 mM KCl, and 6.2 Å in 50 mM CsCl. That is, NPs in CsCl electrolyte are further into the suspension from the AWI than the same NP in LiCl electrolyte by up to several molecular layers. These relative immersion depths hold for all assumed initial depths of the NP in LiCl (bearing in mind the limited probe depth of an XPS experiment).

The diffusion coefficient, calculated from the Stokes−Einstein equation, for a 9 nm particle in 5 wt % suspension at 279 K is on the order of 10^{-11} m^2·s^{-1}. Given the time frame of the LJ experiments, from liquid exit of the quartz nozzle to ionization by X-rays (2 mm downstream at a speed of 7 m/s), 285 μs,[34] a 9 nm particle diffuses ∼10 diameters. We therefore do not expect that the spatial distributions of the NPs, which differ by less than one tenth of a particle diameter, are an artifact of the LJ experiment. Similar results would be expected for static systems (although at present they cannot be measured by XPS).

Surface Tension. We measured the surface tensions of our colloidal samples using a platinum Wilhelmy plate. The NP-induced excess surface pressures, Π, are (essentially) zero for the four different electrolyte suspensions (Figure 2c and Table 1), in full agreement with previous reports[8,9] and consistent with the hydrophilic NPs being fully immersed in the aqueous phase (the NPs do not protrude into the air phase).[9] The strong variation in the XPS Si 2p/O 1s(liq) ratios with electrolyte must therefore reflect changes in the (immediate) subsurface spatial distributions of the NPs at the AWI; these changes go undetected by macroscopic surface tension measurements that are largely sensitive only to the outermost molecular layer of the AWI where the NPs are not located. The relative immersion depth of zero assigned to a NP in LiCl electrolyte (Figure 3) should therefore not be interpreted as meaning the NP is in contact with the AWI, but instead resides (slightly) below the AWI in a fully hydrated state.
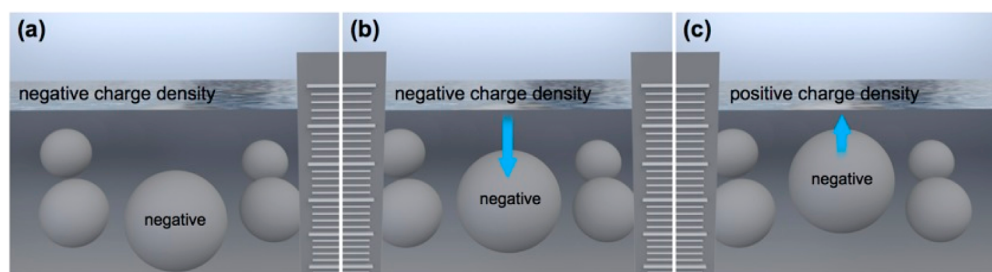
Figure 4. (a) At large separation the air–water interface and the NP do not interact electrostatically. (b) At intermediate distances the negative charge of the NP and the negative charge density of the AWI repel one another. (c) At small separations the AWI becomes polarized by the sufficient negative external potential of the NP and changes its charge density from negative to positive. This charge inversion creates an attractive interaction that results in NPs with higher negative charge approaching the AWI more closely than less negatively charged NPs.

Electrophoretic Mobility and Zeta Potential. The NPs zeta potential (ζ) can be calculated from electrophoretic mobility measurements. The zeta potentials are negative (red circles of Figure 2b and Table 1), in agreement with previous reports,[35] and consistent with a solution pH (10) well above the isoelectric point of SiO_2.[36] The magnitude of the NPs zeta potentials decreases with $|LiCl| > |NaCl| > |KCl| > |CsCl|$, which is believed to result from the poorly hydrated cations (Cs^+ and K^+) adsorbing in greater quantity to the silica NP surface than the well-hydrated ones (Li^+ and Na^+) and thereby providing more effective screening of the NP's surface potential.[35] There is a clear trend between the NP's zeta potentials and their relative concentrations near the AWI (Figure 2b); the different spatial distributions of the NPs at the AWI correlate to the NP's varying electrostatic potentials in the different electrolytes (as the $|\zeta|$ increases so too does the concentration of NPs at the AWI). Electrostatic interactions are therefore expected to determine the equilibrium distance between the NPs and the AWI as measured by XPS.

Surface Charge and Potential of the AWI. The charge (and related electrostatic potential) of the AWI at neutral pH is a controversial topic.[12] While many experiments agree that preferential adsorption of OH^- results in negative surface potential (for example, see refs 37–40), state-of-the-art computational models remain unable to reproduce these findings.[41] In part, the lack of consensus between experiment and theory originates from experiment measuring solutions that contain electrolytes, solutes (reactants), and (unfortunately) impurities, whereas computational models investigate miniscule amounts of pure water.[41] In alkali chloride (more generally alkali halide[42–45]) electrolytes, the picture is more clear. Molecular dynamics simulations,[46–48] X-ray spectroscopy,[48] zeta potentials,[49] and vibrational sum frequency generation[44,50,51] (VSFG) experiments all agree on a distribution at the AWI where the chloride anions (Cl^-) are located above (closer to the air phase) the alkali cations. This uneven distribution creates an ionic double layer and a corresponding gradient from a more negative to a more positive electrostatic potential when crossing from air into water. At pH 10, where the present experiments were performed, the concentration of OH^- exceeds that of H_3O^+ by 10^6 in bulk solution. With a million-fold excess of OH^- (relative to H_3O^+) and in alkali chloride electrolyte (50 mM LiCl, NaCl, KCl, or CsCl), there should be little doubt that the AWI carries negative charge density/potential in our experiments.

Theoretical Model. We propose a theoretical model based on the interaction of two planar parallel surfaces that is able to qualitatively rationalize our experimental findings. The model is based on two assumptions. First, the AWI carries a constant (and fixed) electrostatic potential, Φ_{AWI}, and second, the magnitude of Φ_{AWI} is smaller than that of the NP's negative electrostatic potential, Φ_{NP}, when residing in bulk water. We point out that, generally, in the presence of mobile charge carriers it is the electrochemical potential that remains constant. If the charge carriers on the AWI are able to move without restriction (that is, without entailing a demixing entropy cost and without nonelectrostatic interactions), changes in the chemical potential can be ignored and the charge carriers' electrochemical potential thus depends only on the electrostatic potential. The general equilibrium condition of a constant electrochemical potential then reduces to the more specific condition of a constant electrostatic potential on the AWI. We focus on the case that Φ_{AWI} carries a negative sign, consistent with the aforementioned experimental and molecular dynamics simulation studies in NaCl electrolyte and a bulk pH of 10.[37–39,44,46–48,50,51] Yet, our model remains valid even for positive Φ_{AWI}, given $|\Phi_{NP}| > |\Phi_{AWI}|$.

The predictions of our model, which have been worked out analytically in the framework of Debye–Hückel theory (see Methods), are graphically summarized in Figure 4. At large NP–AWI separations, D, where $D >$ the Debye screening length, l_D, the two surfaces do not interact with each other (Figure 4a). Each surface will form a diffuse double layer of counterions with a characteristic Debye screening length, $l_D =$ 13 Å (at 50 mM monovalent electrolyte), the AWI because of its negative potential and the NP because of its negative surface charge density. As the like-charged NP and AWI approach each other, their diffuse double layers start to overlap, causing repulsion (Figure 4b). The energy barrier to overcome this repulsion is predicted by the Debye–Hückel model to be about 10 k_BT at room temperature for a single NP (see Methods) and is easily surmountable under the conditions of our experiments. When the NP–AWI separation becomes sufficiently small, $D < \tilde{D}$ (where $\tilde{D} \approx l_D$), NP-induced polarization leads to a charge redistribution (reversal) at the AWI. Thus, below $\tilde{D}$ the AWI carries a positive charge density despite its negative potential. At slightly smaller separation, $D = \bar{D} < \tilde{D}$, the induced positive charge density at the AWI is large enough so that electrostatic attraction between the NP and the AWI sets in (Figure 4c).

For very small separations, $D \ll l_D$, the electrostatic attraction will be counterbalanced by a hydration repulsion that decays exponentially with a characteristic length, $\xi = 2$ Å.[18] The interplay between electrostatic attraction and hydration repulsion leads to an equilibrium distance, $D = D^{eq}$, between the NP and the AWI. As demonstrated in Methods, modeling

the electrostatic interactions on the basis of Debye–Hückel theory leads to the equilibrium distance

$$D^{\mathrm{eq}} = -\xi \log(\Phi_{\mathrm{NP}}{}^2 - \Phi_{\mathrm{AWI}}{}^2) - z \qquad (4)$$

where z is a function that depends on the magnitude of the hydration repulsion but is independent of Φ_{NP} and Φ_{AWI}. We regard z as an unknown constant with respect to which the equilibrium distance is measured. In the present experiments both Φ_{NP} (zeta potential, Figure 2b and Table 1) and $\Phi_{\mathrm{AWI}}{}^{46-48,50,51}$ are negative, and according to eq 4, the more negative Φ_{NP} is with respect to Φ_{AWI} the smaller is D^{eq}. Because a more negative zeta potential of the NP implies a more negative Φ_{NP}, we find eq 4 in qualitative agreement with the XPS results of Figure 3. We point out again that even if Φ_{AWI} were positive, eq 4 would still qualitatively reproduce our XPS results because the electrostatic potentials enter quadratically.

A quantitative comparison may be attempted[52] by taking the zeta potential, ζ, as being proportional to the surface potential, $\Phi_{\mathrm{NP}} = w\zeta$, where $w > 1$ is a constant that accounts for the adsorption of electrolyte ions within the region inside (or at) the hydrodynamic shear plane. Because $\zeta = \Phi_{\mathrm{NP}}\, e^{-(d/l_{\mathrm{D}})}$, the distance between the two surfaces to which Φ_{NP} and ζ refer is $d = l_{\mathrm{D}} \log(w)$. When the values $z = -15.4$ Å, $w = 1.28$, and $\Phi_{\mathrm{AWI}} = -50$ mV are chosen, our model predicts SiO_2 NP immersion depths of $D^{\mathrm{eq}} = 1.02$ Å in 50 mM NaCl, $D^{\mathrm{eq}} = 2.24$ Å in 50 mM KCl, and $D^{\mathrm{eq}} = 6.20$ Å in 50 mM CsCl, all relative to a NP in 50 mM LiCl (where D^{eq} has been set to zero by the choice of z and w). The relation between the NP's zeta potential and D^{eq} for the Debye–Hückel model are shown together with the experimental XPS results in Figure 3. Excellent agreement between theory (solid line) and experiment (markers) is observed, with negligible influence of the exact choice of Φ_{AWI} on the quality of the fit.

DISCUSSION

At separations less than one Debye screening length in solution, our work suggests that the electric field of a charged NP (when $|\Phi_{\mathrm{NP}}| > |\Phi_{\mathrm{AWI}}|$) is sufficient to induce a local redistribution of the ions at the AWI that inverts its negative charge density to positive. This induced positive charge density at the AWI plays a prominent role in regulating NP spatial distributions: more negatively charged NPs are attracted closer to the AWI than similar NPs with less charge. These findings provide evidence that microscopic control over NP spatial distributions, with a resolution of a single molecular layer, can be realized at the AWI by either varying the size of NP in solution,[53−55] by changes to bulk solution pH[56,57] or electrolyte (this work), or by varying the electrolyte concentration,[35] all of which have been shown to influence NPs surface charge/zeta potential/ surface potential in aqueous solutions.

Previous experimental efforts to quantify the spatial distributions of oxide NPs at the AWI are limited. Only two such spectroscopic reports exist, one using X-ray reflectivity for 8 nm Fe_2O_3[58] and a second by X-ray photoelectron spectroscopy for 3 nm SnO_2.[31] Both measurements revealed that the NPs are excluded from the interface by up to several molecular layers of water, largely thought to originate from electrostatic *repulsion* between the negatively charged NPs and the negative potential-carrying AWI. However, these studies, while instrumental in their spectroscopic approach, did not systematically vary parameters (like electrolyte) that would have allowed for the more detailed descriptions provided herein. Nevertheless, their conclusions that negatively charged NPs are excluded from the AWI are confirmed here, although with the interpretation that this is not a result of electrostatic *repulsion*, but the consequence of interplay between electrostatic attraction and a nonelectrostatic repulsion. The former results from the mobility of the charge carriers at the AWI, whereas the latter from hydration repulsion due to the mutual perturbation of ordered water molecules close to the NP and the AWI.

Our results can be generalized for two sets of conditions. In the first, $|\Phi_{\mathrm{NP}}| > |\Phi_{\mathrm{AWI}}|$ and the NPs, irrespective of the sign (positive or negative) of their surface potential, will be electrostatically attracted to the AWI. In aqueous solutions where the AWI has negative surface charge density (generally thought for pH > 2–3[40,49,59]), negatively charged NPs will induce a charge redistribution (to positive charge density), whereas in the presence of positively charged NPs the AWI will remain negatively charged. In both cases electrostatic attraction prevails. In highly acidic solutions (pH < 2), the AWI will have positive surface charge density (excess H_3O^+) and again both positive and negatively charged NPs will be electrostatically attracted. In this case, positive NPs will induce a charge redistribution at the AWI that inverts the positive charge density to negative (a situation that is analogous to that at high pH studied herein). In the second, $|\Phi_{\mathrm{NP}}| < |\Phi_{\mathrm{AWI}}|$ and the electric field of the NP is insufficient to induce a charge redistribution of the AWI. Under these conditions, like charges of the AWI and NP will repel, whereas opposite charges will attract one another. At pH close to the NPs isoelectric point (pH where the particle has zero charge) are the only conditions where we anticipate $|\Phi_{\mathrm{NP}}| < |\Phi_{\mathrm{AWI}}|$ being of significance for oxide NPs in aqueous solutions. Finally, with the AWI serving as a general model for hydrophilic–hydrophobic interfaces, our findings are expected to also describe the general behavior of charge-stabilized NPs and their spatial distributions at aqueous–oil interfaces.

CONCLUSIONS

The subsurface spatial distributions of colloidal NPs near the AWI have been quantitatively determined using a combination of XPS from a liquid microjet, electrophoretic mobility, and surface tension measurements. The surprising attraction of the negatively charged NPs to the AWI under conditions where the AWI is known to have negative potential (at pH > 3 and in alkali chloride electrolytes) stems uniquely from a NP-induced charge redistribution of the AWI that inverts its negative charge density to positive. A Debye–Hückel model for the interaction between a planar NP surface and the AWI qualitatively reproduces the experimental observations of XPS that specific cation effects, which serve to control the NP interfacial potential, regulate the spatial distributions of the NPs near the AWI through attractive electrostatic forces with the AWI.

The negative surface charge density (and its related electrostatic potential) of the AWI has profound implications in a wide variety of contexts,[12] in particular for gas–liquid chemical reactions in atmospheric sciences,[39,42,43,60] and is thought to be nontrivial to invert through changes in bulk pH,[39,59] electrolyte,[59] and electrolyte strength.[38,59] To our knowledge, there has been no study, either experimental or theoretical, that has shown the charge at the AWI can be reversed, polarized, or inverted under any specific conditions other than by acidifying the solution to pH < 2−3.[40,49,59] Through a combination of experiment and theory our results

reveal that in the close approach of a negatively charged NP the AWI inverts its negative charge density to positive. This charge inversion will have profound consequences on chemical reaction rates and product distributions in gas−liquid reactions.[39,42,43]

X-ray photoelectron spectroscopy from a liquid microjet has great potential to provide a complete microscopic description of NPs in liquid solutions.[24] Combining information on the spatial distribution of particles, as we have done here, with electronic structure information concerning the NPs surface potential, as has been recently demonstrated,[56] complete spatial and electronic detail heretofore impossible with any one other analytical method[61] will be realized. Microscopic detail at this level will provide immediate benefit to researchers in soft-matter physics, nanomedicine, nanotechnology, and (geo-) chemistry.

■ ASSOCIATED CONTENT

Ⓢ Supporting Information

Experimental details; results of TEM, SAXS, and XRD experiments; and calculated photoelectron signal as a function of nanoparticle immersion depth. This material is available free of charge via the Internet at http://pubs.acs.org.

■ AUTHOR INFORMATION

Corresponding Author
*E-mail: matthew.brown@mat.ethz.ch. Tel: +41 44 632 3048.

Notes
The authors declare no competing financial interest.

■ ACKNOWLEDGMENTS

■ REFERENCES

(1) Binks, B. P. Particles as Surfactants—Similarities and Differences. *Curr. Opin. Colloid Interface Sci.* **2002**, *7*, 21−41.

(2) Aveyard, R.; Binks, B. P.; Clint, J. H. Emulsions Stabilised Solely by Colloidal Particles. *Adv. Colloid Interface Sci.* **2003**, *100*, 503−546.

(3) Binks, B. P.; Horozov, T. S. Aqueous Foams Stabilized Solely by Silica Nanoparticles. *Angew. Chem., Int. Ed.* **2005**, *44*, 3722−3725.

(4) Pietra, F.; Rabouw, F. T.; Evers, W. H.; Byelov, D. V.; Petukhov, A. V.; Donega, C. D.; Vanmaekelbergh, D. Semiconductor Nanorod Self-Assembly at the Liquid/Air Interface Studied by in Situ GISAXS and ex Situ TEM. *Nano Lett.* **2012**, *12*, 5515−5523.

(5) Dong, A.; Jiao, Y.; Milliron, D. J. Electronically Coupled Nanocrystal Superlattice Films by in situ Ligand Exchange at the Liquid-Air Interface. *ACS Nano* **2013**, *7*, 10978−10984.

(6) Boker, A.; He, J.; Emrick, T.; Russell, T. P. Self-Assembly of Nanoparticles at Interfaces. *Soft Matter* **2007**, *3*, 1231−1248.

(7) Butt, H.-J.; Graf, K.; Kappl, M. *Physics and Chemistry of Interfaces*, 3rd ed.; Wiley-VCH Verlag GmbH & Company: Weinheim, Germany, 2013.

(8) Blute, I.; Pugh, R. J.; van de Pas, J.; Callaghan, I. Industrial Manufactured Silica Nanoparticle Sols. 2: Surface Tension, Particle Concentration, Foam Generation and Stability. *Colloids Surf., A* **2009**, *337*, 127−135.

(9) Brown, M. A.; Duyckaerts, N.; Beloqui Redondo, A.; Jordan, I.; Nolting, F.; Kleibert, A.; Ammann, M.; Wörner, H. J.; van Bokhoven, J. A.; Abbas, Z. Effect of Surface Charge Density on the Affinity of Oxide Nanoparticles for the Vapor−Water Interface. *Langmuir* **2013**, *29*, 5023−5029.

(10) van Rijssel, J.; van der Linden, M.; Meeldijk, J. D.; van Dijk-Moes, R. J. A.; Philipse, A. P.; Erne, B. H. Spatial Distribution of Nanocrystals Imaged at the Liquid-Air Interface. *Phys. Rev. Lett.* **2013**, *111*, 108302.

(11) Shrestha, A.; Bohinc, K.; May, S. Immersion Depth of Positively versus Negatively Charged Nanoparticles at the Air-Water Interface: A Poisson-Boltzmann Model. *Langmuir* **2012**, *28*, 14301−14307.

(12) Saykally, R. J. Air/Water Interface: Two Sides of the Acid-Base Story. *Nat. Chem.* **2013**, *5*, 82−84.

(13) Gitlin, I.; Carbeck, J. D.; Whitesides, G. M. Why are Proteins Charged? Networks of Charge-Charge Interactions in Proteins Measured by Charge Ladders and Capillary Electrophoresis. *Angew. Chem., Int. Ed.* **2006**, *45*, 3022−3060.

(14) Gidalevitz, D.; Huang, Z. Q.; Rice, S. A. Protein Folding at the Air-Water Interface Studied with X-Ray Reflectivity. *Proc. Natl. Acad. Sci. U.S.A.* **1999**, *96*, 2608−2611.

(15) Winter, B.; Faubel, M. Photoemission from Liquid Aqueous Solutions. *Chem. Rev. (Washington, DC, U.S.)* **2006**, *106*, 1176−1211.

(16) Pruyne, J. G.; Lee, M.-T.; Fábri, C.; Beloqui Redondo, A.; Kleibert, A.; Ammann, M.; Brown, M. A.; Krisch, M. J. Liquid−Vapor Interface of Formic Acid Solutions in Salt Water: A Comparison of Macroscopic Surface Tension and Microscopic in Situ X-ray Photoelectron Spectroscopy. *J. Phys. Chem. C* **2014**, *118*, 29350−29360.

(17) Fennell Evans, D.; Wennerström, H. *The Colloidal Domain: Where Physics, Chemistry, Biology and Technology Meet.*, 2nd ed.; Wiley-VCH: New York, 1999.

(18) Marcelja, S. Hydration Forces Near Charged Interfaces in Terms of Effective Ion Potentials. *Curr. Opin. Colloid Interface Sci.* **2011**, *16*, 579−583.

(19) Chen, X. J.; Jiang, J. G.; Yan, F.; Tian, S. C.; Li, K. M. A Novel Low Temperature Vapor Phase Hydrolysis Method for the Production of Nano-Structured Silica Materials using Silicon Tetrachloride. *RSC Adv.* **2014**, *4*, 8703−8710.

(20) Lis, D.; Backus, E. H. G.; Hunger, J.; Parekh, S. H.; Bonn, M. Liquid Flow Along a Solid Surface Reversibly Alters Interfacial Chemistry. *Science* **2014**, *344*, 1138−1142.

(21) Tan, W. H.; Wang, K. M.; He, X. X.; Zhao, X. J.; Drake, T.; Wang, L.; Bagwe, R. P. Bionanotechnology Based on Silica Nanoparticles. *Med. Res. Rev.* **2004**, *24*, 621−638.

(22) Ambrogio, M. W.; Thomas, C. R.; Zhao, Y. L.; Zink, J. I.; Stoddartt, J. F. Mechanized Silica Nanoparticles: A New Frontier in Theranostic Nanomedicine. *Acc. Chem. Res.* **2011**, *44*, 903−913.

(23) Rose, S.; Prevoteau, A.; Elziere, P.; Hourdet, D.; Marcellan, A.; Leibler, L. Nanoparticle Solutions as Adhesives for Gels and Biological Tissues. *Nature* **2014**, *505*, 382−385.

(24) Brown, M. A.; Jordan, I.; Beloqui Redondo, A.; Kleibert, A.; Wörner, H. J.; van Bokhoven, J. A. In Situ Photoelectron Spectroscopy at the Liquid/Nanoparticle Interface. *Surf. Sci.* **2013**, *610*, 1−6.

(25) Brown, M. A.; Beloqui Redondo, A.; Jordan, I.; Duyckaerts, N.; Lee, T. M.; Ammann, M.; Nolting, F.; Kleibert, A.; Machler, J. P.; Birrer, M.; et al. A New Endstation at the Swiss Light Source for Ultraviolet Photoelectron Spectroscopy, X-ray Photoelectron Spectroscopy, and X-ray Absorption Spectroscopy Measurements of Liquid Solutions. *Rev. Sci. Instrum.* **2013**, *84*, 073904.

(26) Flechsig, U.; Nolting, F.; Rodriguez, A. F.; Krempasky, J.; Quitmann, C.; Schmidt, T.; Spielmann, S.; Zimoch, D. Performance

Measurements at the SLS SIM Beamline. *AIP Conf. Proc.* **2010**, *1234*, 319−322.

(27) Brown, M. A.; Seidel, R.; Thurmer, S.; Faubel, M.; Hemminger, J. C.; van Bokhoven, J. A.; Winter, B.; Sterrer, M. Electronic Structure of Sub-10 nm Colloidal Silica Nanoparticles Measured by In Situ Photoelectron Spectroscopy at the Aqueous-Solid Interface. *Phys. Chem. Chem. Phys.* **2011**, *13*, 12720−12723.

(28) Brown, M. A.; Winter, B.; Faubel, M.; Hemminger, J. C. Spatial Distribution of Nitrate and Nitrite Anions at the Liquid/Vapor Interface of Aqueous Solutions. *J. Am. Chem. Soc.* **2009**, *131*, 8354−8355.

(29) Brown, M. A.; Arrigoni, M.; Heroguel, F.; Beloqui Redondo, A.; Giordano, L.; van Bokhoven, J. A.; Pacchioni, G. pH Dependent Electronic and Geometric Structures at the Water-Silica Nanoparticle Interface. *J. Phys. Chem. C* **2014**, *118*, 29007−29016.

(30) Ashley, J. C.; Anderson, V. E. Interaction of Low-Energy Electrons with Silicon Dioxide. *J. Electron Spectrosc. Relat. Phenom.* **1981**, *24*, 127−148.

(31) Jordan, I.; Beloqui Redondo, A.; Brown, M. A.; Fodor, D.; Staniuk, M.; Kleibert, A.; Wörner, H. J.; Giorgi, J. B.; van Bokhoven, J. A. Non-Uniform Spatial Distribution of Tin Oxide (SnO_2) Nanoparticles at the Air-Water Interface. *Chem. Commun. (Cambridge, U.K.)* **2014**, *50*, 4242−4244.

(32) Ottosson, N.; Faubel, M.; Bradforth, S. E.; Jungwirth, P.; Winter, B. Photoelectron Spectroscopy of Liquid Water and Aqueous Solution: Electron Effective Attenuation Lengths and Emission-Angle Anisotropy. *J. Electron Spectrosc. Relat. Phenom.* **2010**, *177*, 60−70.

(33) Thurmer, S.; Seidel, R.; Faubel, M.; Eberhardt, W.; Hemminger, J. C.; Bradforth, S. E.; Winter, B. Photoelectron Angular Distributions from Liquid Water: Effects of Electron Scattering. *Phys. Rev. Lett.* **2013**, *111*, 173005.

(34) Smolentsev, N.; Chen, Y.; Jena, K. C.; Brown, M. A.; Roke, S. Sum Frequency and Second Harmonic Generation from the Surface of a Liquid Microjet. *J. Chem. Phys.* **2014**, *141*, 18C524.

(35) Franks, G. V. Zeta Potentials and Yield Stresses of Silica Suspensions in Concentrated Monovalent Electrolytes: Isoelectric Point Shift and additional Attraction. *J. Colloid Interface Sci.* **2002**, *249*, 44−51.

(36) Bolt, G. H. Determination of the Charge Density of Silica Sols. *J. Phys. Chem.* **1957**, *61*, 1166−1169.

(37) Beattie, J. K.; Djerdjev, A. N.; Warr, G. G. The Surface of Neat Water is Basic. *Faraday Discuss.* **2009**, *141*, 31−39.

(38) Gehring, T.; Fischer, T. M. Diffusion of Nanoparticles at an Air/Water Interface Is Not Invariant under a Reversal of the Particle Charge. *J. Phys. Chem. C* **2011**, *115*, 23677−23681.

(39) Mishra, H.; Enami, S.; Nielsen, R. J.; Stewart, L. A.; Hoffmann, M. R.; Goddard, W. A.; Colussi, A. J. Bronsted Basicity of the Air-Water Interface. *Proc. Natl. Acad. Sci. U.S.A.* **2012**, *109*, 18679−18683.

(40) Takahashi, M. ζ Potential of Microbubbles in Aqueous Solutions: Electrical Properties of the Gas-Water interface. *J. Phys. Chem. B* **2005**, *109*, 21858−21864.

(41) Baer, M. D.; Kuo, I. F. W.; Tobias, D. J.; Mundy, C. J. Toward a Unified Picture of the Water Self-Ions at the Air-Water Interface: A Density Functional Theory Perspective. *J. Phys. Chem. B* **2014**, *118*, 8364−8372.

(42) Hu, J. H.; Shi, Q.; Davidovits, P.; Worsnop, D. R.; Zahniser, M. S.; Kolb, C. E. Reactive Uptake of $Cl_2(g)$ and $Br_2(g)$ by Aqueous Surfaces as a Function of Br- and I- Ion Concentration - the Effect of Chemical-Reaction at the Interface. *J. Phys. Chem.* **1995**, *99*, 8768−8776.

(43) Knipping, E. M.; Lakin, M. J.; Foster, K. L.; Jungwirth, P.; Tobias, D. J.; Gerber, R. B.; Dabdub, D.; Finlayson-Pitts, B. J. Experiments and Simulations of Ion-Enhanced Interfacial Chemistry on Aqueous NaCl Aerosols. *Science* **2000**, *288*, 301−306.

(44) Piatkowski, L.; Zhang, Z.; Backus, E. H. G.; Bakker, H. J.; Bonn, M. Extreme Surface Propensity of Halide Ions in Water. *Nat. Commun.* **2014**, *5*, 4083.

(45) Netz, R. R.; Horinek, D. Progress in Modeling of Ion Effects at the Vapor/Water Interface. *Annu. Rev. Phys. Chem.* **2012**, *63*, 401−418.

(46) Wick, C. D.; Dang, L. X.; Jungwirth, P. Simulated Surface Potentials at the Vapor-Water Interface for the KCl Aqueous Electrolyte Solution. *J. Chem. Phys.* **2006**, *125*, 024706.

(47) Ishiyama, T.; Morita, A. Molecular Dynamics Study of Gas-Liquid Aqueous Sodium Halide Interfaces. I. Flexible and Polarizable Molecular Modeling and Interfacial Properties. *J. Phys. Chem. C* **2007**, *111*, 721−737.

(48) Cheng, M. H.; Callahan, K. M.; Margarella, A. M.; Tobias, D. J.; Hemminger, J. C.; Bluhm, H.; Krisch, M. J. Ambient Pressure X-ray Photoelectron Spectroscopy and Molecular Dynamics Simulation Studies of Liquid/Vapor Interfaces of Aqueous NaCl, RbCl, and RbBr Solutions. *J. Phys. Chem. C* **2012**, *116*, 4545−4555.

(49) Li, C.; Somasundaran, P. Reversal of Bubble Charge in Multivalent Inorganic Salt-Solutions—Effect of Magnesium. *J. Colloid Interface Sci.* **1991**, *146*, 215−218.

(50) Tian, C. S.; Byrnes, S. J.; Han, H. L.; Shen, Y. R. Surface Propensities of Atmospherically Relevant Ions in Salt Solutions Revealed by Phase-Sensitive Sum Frequency Vibrational Spectroscopy. *J. Phys. Chem. Lett.* **2011**, *2*, 1946−1949.

(51) Hua, W.; Verreault, D.; Huang, Z. S.; Adams, E. M.; Allen, H. C. Cation Effects on Interfacial Water Organization of Aqueous Chloride Solutions. I. Monovalent Cations: Li^+, Na^+, K^+, and NH_4^+. *J. Phys. Chem. B* **2014**, *118*, 8433−8440.

(52) The linearized Debye−Hückel model is restricted to potentials of absolute values smaller than 25 mV. Here both the AWI and NP have potentials greater than that.

(53) Abbas, Z.; Labbez, C.; Nordholm, S.; Ahlberg, E. Size-Dependent Surface Charging of Nanoparticles. *J. Phys. Chem. C* **2008**, *112*, 5715−5723.

(54) Brown, M. A.; Huthwelker, T.; Beloqui Redondo, A.; Janousch, M.; Faubel, M.; Arrell, C. A.; Scarongella, M.; Chergui, M.; van Bokhoven, J. A. Changes in the Silanol Protonation State Measured In Situ at the Silica-Aqueous Interface. *J. Phys. Chem. Lett.* **2012**, *3*, 231−235.

(55) Barisik, M.; Atalay, S.; Beskok, A.; Qian, S. Z. Size Dependent Surface Charge Properties of Silica Nanoparticles. *J. Phys. Chem. C* **2014**, *118*, 1836−1842.

(56) Brown, M. A.; Beloqui Redondo, A.; Sterrer, M.; Winter, B.; Pacchioni, G.; Abbas, Z.; van Bokhoven, J. A. Measure of Surface Potential at the Aqueous−Oxide Nanoparticle Interface by XPS from a Liquid Microjet. *Nano Lett.* **2013**, *13*, 5403−5407.

(57) Atalay, S.; Ma, Y.; Qian, S. Z. Analytical Model for Charge Properties of Silica Particles. *J. Colloid Interface Sci.* **2014**, *425*, 128−130.

(58) Paulus, M.; Degen, P.; Schmacke, S.; Maas, M.; Kahner, R.; Struth, B.; Tolan, M.; Rehage, H. In Situ Observation of Maghemite Nanoparticle Adsorption at the Water/Gas Interface. *Eur. Phys. J.: Spec. Top.* **2009**, *167*, 133−136.

(59) Creux, P.; Lachaise, J.; Graciaa, A.; Beattie, J. K.; Djerdjev, A. M. Strong Specific Hydroxide Ion Binding at the Pristine Oil/Water and Air/Water Interfaces. *J. Phys. Chem. B* **2009**, *113*, 14146−14150.

(60) Ghosal, S.; Hemminger, J. C.; Bluhm, H.; Mun, B. S.; Hebenstreit, E. L. D.; Ketteler, G.; Ogletree, D. F.; Requejo, F. G.; Salmeron, M. Electron Spectroscopy of Aqueous Solution Interfaces Reveals Surface Enhancement of Halides. *Science* **2005**, *307*, 563−566.

(61) Zaera, F. Probing Liquid/Solid Interfaces at the Molecular Level. *Chem. Rev. (Washington, DC, U.S.)* **2012**, *112*, 2920−2986.